CFSRC COLLOQUIUM

Proceedings of the Cold-Formed Steel Research Consortium Colloquium
20-22 October 2020 (cfsrc.org)

Study on Section Capacity of Stainless Steel Lipped-C Beam-Columns

Kang Han[1], Yueming Yang[2], Shuang Niu[3]

Abstract

This paper aims to explore the buckling behavior and the section capacity of cold-formed stainless steel lipped-C stub beam-columns under combined axial compression and uniaxial bending. A total of 24 stub columns were tested comprising two sets of sections designed to fail by distortional buckling mode and local buckling mode respectively. Two alloys, austenitic S30401 and duplex S32205, were employed in the experiments. Three loading eccentricity levels (none, small and large) were designed to produce different stress gradients within the tested sections. Refined finite element models were established with ABAQUS and validated with the detailed test results. A systematic geometric and material nonlinear analysis were then carried out covering two alloys, four plate thicknesses, four local/distortional buckling slenderness levels and five loading eccentricity levels. Lastly, based on the current Direct Strength Method (DSM) design expression, the modified expression for the section capacity prediction was proposed which suits both stainless steel columns and beam-columns of lipped-C sections.

1. General

Structural stainless steel earns a highly praised reputation in structural application, thanks to its preeminent corrosion resistance, easy maintenance, fine fire resistance and attractive appearance, etc. Considerable progress, as reviewed by Gardner [1], Baddoo [2] and Gedge [3], greatly promotes the application of structural stainless steel over the past two decades. Meanwhile, high material cost and nonlinear material properties have made it the biggest obstacle for its application. Cold-formed thin-walled members bear a higher level of strength-to-weight ratio and rigidity-to-weight ratio, they also possess a high level of cold hardening effect and material utilization [4]. These characteristics are especially suitable for the high-cost stainless steel material.

However, the buckling behaviors of cold-formed stainless steel tend towards complexity due to great diversities of section forms, different buckling modes (see Figure 1) and profound nonlinear constitutive relation of the material (see Figure 2), which needs a further investigation. Moreover, for design of beam-columns, almost all current design specifications employ the unified, simplified linear interaction expression based on combining isolated axial and bending strength response, which tends to be conservative [5], and in some specifications, the bearing performance of various sections with different buckling characteristics, such as distortional buckling, was not taken into consideration.

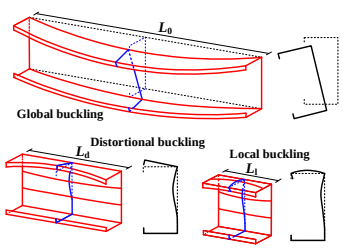

Figure 1 Buckling modes

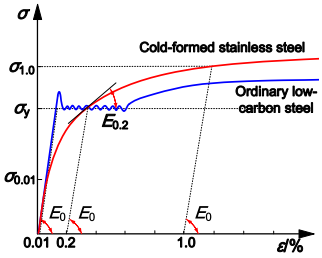

Figure 2 Nonlinear constitutive relation [6]

Stub columns refer to the members failed only by sectional buckling under actions, and the global buckling and the second-order effect are not taken into consideration. The stability coefficients of stub columns are very close to 1. The buckling behaviors and characteristics can lay a foundation for the investigation of long columns. 37 stub column tests containing square, rectangular and circular hollow sections were conducted by Gardner and Nethercot [7] to provide with reference for a new design method. Stub Lipped-C columns were investigated by Lecce [8] before the long column tests. The stainless steel stub columns referring three materials and two kinds of sections were tested by Becque [9] when studying the local-global interaction bucking of the columns. Cold-formed steel lipped-C columns

[1] Graduate Research Assistant, School of Civil Engineering, Harbin Institute of Technology, kanghan3705@outlook.com
[2] Graduate Research Assistant, School of Civil Engineering, Harbin Institute of Technology, tumuyym@126.com
[3] Assistant Professor, School of Civil Engineering, Harbin Institute of Technology, aniu216@126.com

under different actions were carried out by Torabian and Schafer [5] to establish the new DSM expressions.

This paper aims to systematically explore the buckling behaviors, section capacity and influence parameters of cold-formed stainless steel lipped-C stub beam-columns through experimental investigation, numerical study and theoretical study. The section capacity expression which suits the lipped-C stub beam-columns were proposed based on the current Direct Strength Method expressions.

2. Test Design and Test phenomena

2.1 Coupon Tests

Two alloys, namely austenitic S30401 (EN1.4301) and duplex S32205 (EN1.4462) stainless steel (hereinafter referred to as Mat304 and Mat2205, respectively) were employed in the tests. The test members were made from the 2.4m × 1.2m stainless steel sheets. The sheets were first cut into strip and then press-braked into specimens.

The coupon tests were designed according to the material characteristics, including anisotropy, differences in tension and compression performance [10], remarkable strain hardening effect at corner areas. Accordingly, flat coupons were cut from virgin flat sheets along the longitudinal (L), diagonal (45°, D) and transverse (T) direction, and were tested in both tension and compression, as presented in Figure 3. Corner coupons were cut from the 90°-bended sheets and were tested in tension. The parallel coupons were set for each case. The engineering stress-strain curves of Mat304 combined by tensile and compressive coupon test results were shown in Figure 4, in which "304-D-2" represents the parallel test of diagonal coupon with Mat304.

a) Flat coupons in tension b) Flat coupons in compression

Figure 3 Coupon test arrangements

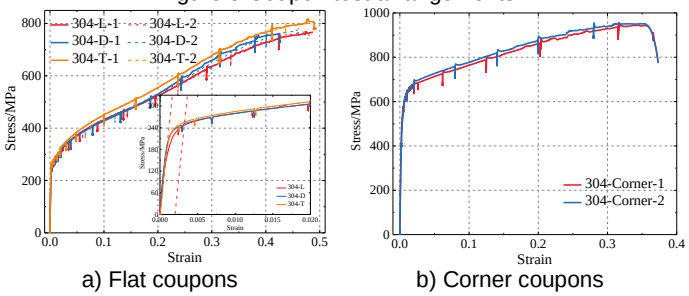

a) Flat coupons b) Corner coupons

Figure 4 Coupon test results of Mat304

2.2 Section Selection

The design goals of the two sections are: Under three given loading eccentricity levels (axial compression, small and large eccentricity), one section tested under combined axial compression and major axis bending and then to fail by distortional buckling (named Section A), the other section tested under combined axial compression and minor axis bending and then to fail by local buckling (named Section B). Two sets of sections were designed by CUFSM [11]. All members were named following the naming scheme shown in Figure 5. The parallel tests were conducted for each eccentricity condition. The definitions of specimen parameters were illustrated in Figure 6.

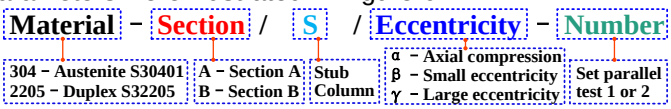

Figure 5 Naming scheme of the test members

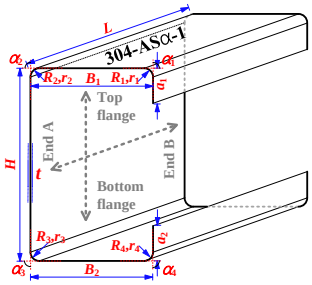

Figure 6 Parameter definitions of lipped-C stub column

Three loading eccentricity levels were selected in tests to produce different stress gradients within two kinds of tested sections. Different eccentricity conditions can be defined according to the ratio of the minimum stress to the maximum stress. The ratios of axial compression, small and large eccentricity are 1, 0.5 and 0, respectively. The design results of nominal dimensions were listed in Table 1. Some design results by CUFSM and the loading locations were shown in Figure 7 and Figure 8. Tensile stress didn't appear within the two designed sections.

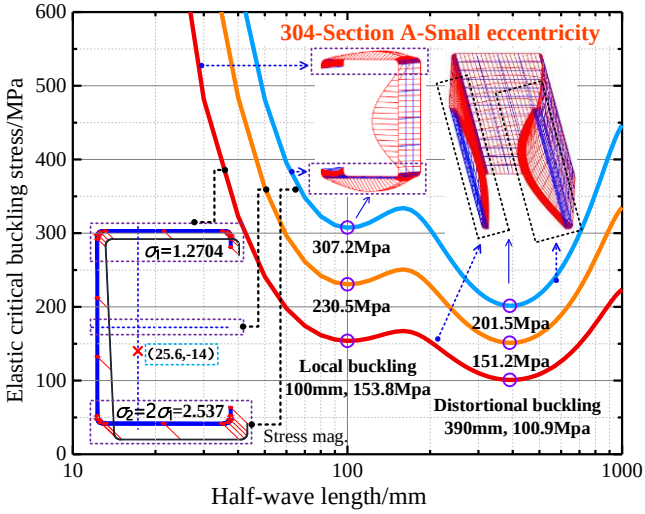

Figure 7 Design result of Section A under small eccentricity

Table 1 Nominal dimensions of Section A and Section B (Unit: mm)

Section types	H	B	a	t	R	L
Section A	120	80	10	1.85	4.0	300
Section B	150	60	20	1.85	4.0	300

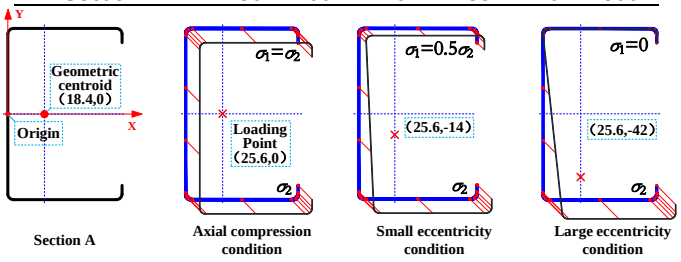

Figure 8 Loading positions of Section A

The actual measurements for all test members were conducted according to the section parameters listed above. The measuring results were all satisfy the design requirements when reexamining through CUFSM.

2.3 Initial Geometric Imperfection

A high-precise measuring equipment with laser displacement meters was set up, which is shown in Figure 9. By these devices, the laser displacement meters can move at a uniform speed along the two rectilinear guides. The distance between laser displacement meters and the member surface can therefore be measured and recorded. The straightness of the two parallel, equal-height rectilinear guides were reexamined before the formal measurements.

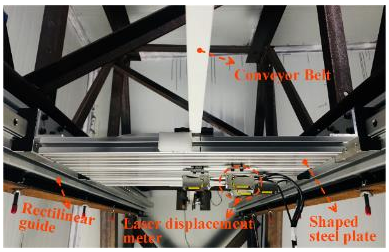

Figure 9 Imperfection measuring equipment

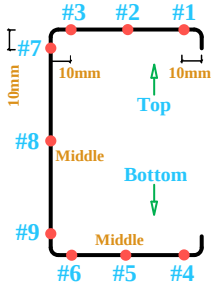

Figure 10 Numbers and positions for imperfection measurement

The numbers and positions of nine measuring channels were listed in Figure 10. All test members were measured from End A to End B with a sampling frequency of 55.86Hz. About 160 points were obtained within the 300mm length of the test member.

Several operations were conducted as the following procedures to process the data. Firstly, let head and tail records return to zero through a linear transform, which is shown in Figure 11. Then deal with the noise of the data and finally, transform the discrete imperfection readings to continuous functions through Fourier fitting. The nine channels of 304-ASα-1 obtained through the processes mentioned above can be seen in Figure 12.

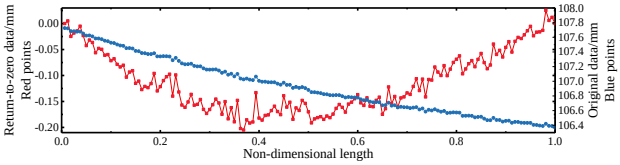

Figure 11 Linear transformation

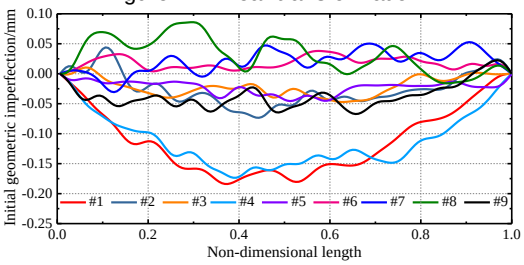

Figure 12 Processed imperfection records of 304-ASα-1

For stub columns, the initial imperfection can be divided into local imperfection and global imperfection, which can be simplified as Figure 13.

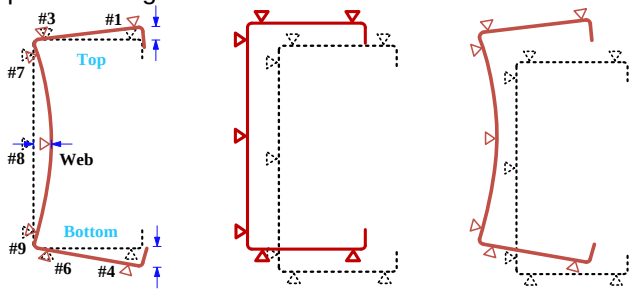

a) Local imperfection b) Global imperfection c) Initial imperfection

Figure 13 Initial geometric imperfection

Channel #3, #6, #7, #9 can be used to represent the global imperfection, and some ratios of the global imperfection amplitude to the effective length of the test members (L_0=550mm) were shown in Figure 14. It has been studied that [12] the local imperfection amplitude of the member can be presented as a function that related to section thickness t and section slenderness λ. In this study, some ratios of the local imperfection amplitudes to their corresponding λt were shown in Figure 15. It can be shown from the measuring results of a total of 24 stub columns that, most global imperfection amplitudes were within the range of 0.2‰ times (L_0/5000) of its effective length; most local imperfection amplitudes were less than $0.08\lambda t$.

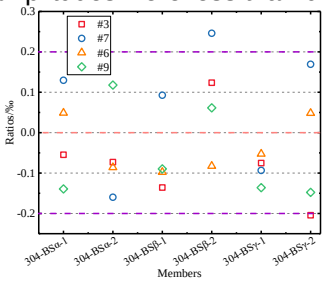

Figure 14 Some global imperfection amplitudes

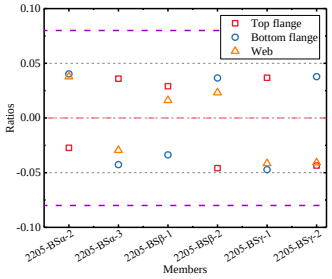

Figure 15 Some local imperfection amplitudes

2.4 Overall arrangement of the test rig

The loading devices with unidirectional swivel joints at both ends were designed for the tests, as shown in Figure 16. The top and bottom loading devices were distributed symmetrically. High-strength gypsum was employed to fix the two ends of the stub column and connect them to the loading plates. The effective lengths of the specimens were the distance between two swivel joints, that is, the effective length of all tested members in this study was 550mm (L_0=550mm).

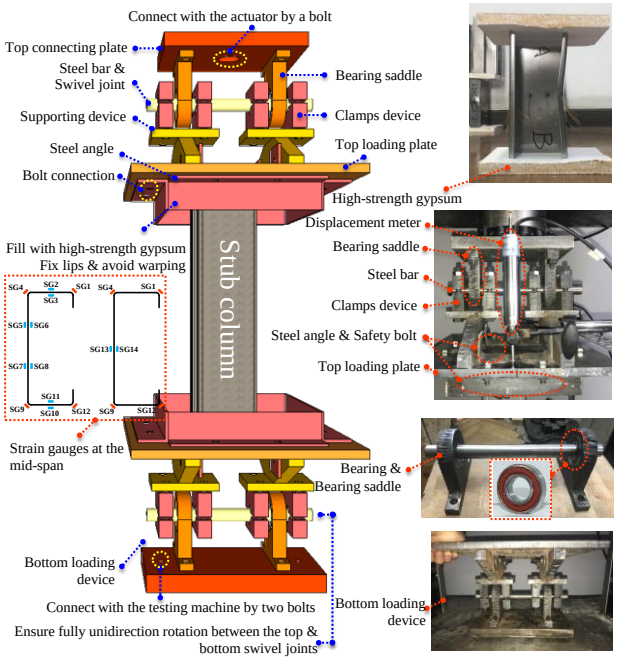

Figure 16 Loading devices

Four displacement meters were arranged on the top and bottom loading plates to accurately describe the change of compressive displacements and rotation angles of the test members. Five displacement meters were arranged at the mid-span section of the test members to monitor the section deformation. The strain gauges were also employed to record the strain variations at the specific areas of the mid-span. Two different strain gauge arrangement schemes were adopted for two parallel test members the schemes were shown in Figure 16.

Simplified finite element models were established by Abaqus to preliminary estimate the section capacity before the formal tests. The members with a predicted section capacity less than 100kN were loaded on the universal testing machine, and that higher than 100kN were loaded on the MTS company's 2500kN electro-hydraulic servo testing machine. The loading rate is firstly taken as 0.1mm/min, and then changed to 0.05mm/min when the force reaching to 80% of the members' estimated section capacity, so as to make the section plasticity fully developed. Figure 17 presents the overall arrangement of one test rig.

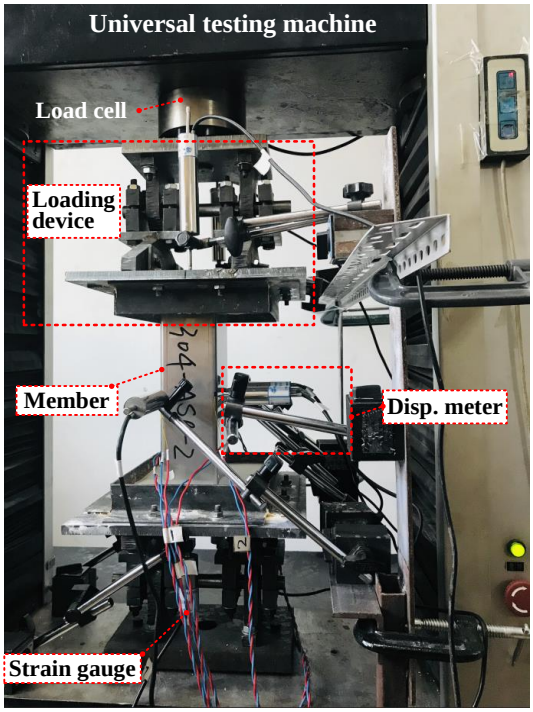

Figure 17 Overall test rig of one loading systems

2.5 Test phenomena

A total of 24 stainless steel lipped-C stub beam-columns were tested under combined axial compression and uniaxial bending, referring to 12 members with Section A and 12 members with Section B. Among them, distortional buckling and local buckling, which is shown in Figure 18 and Figure19, dominated the buckling modes of the members with Section A and Section B under the three loading eccentricity levels, respectively. All of the 24 test members achieved their expected buckling modes.

Figure 18 Distortional buckling of members with Section A

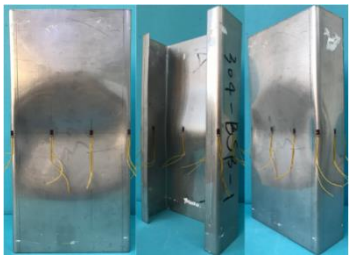

Figure 19 Local buckling of members with Section B

3. FE models and verification

3.1 The arrangements of the FE models

The refined FE models of cold-formed stainless steel lipped-C stub members under combined axial compression and uniaxial bending were established and calibrated through finite element analysis software ABAQUS in this subsection.

3.1.1 Basic settings

Element type: The S4R shell element was selected to establish the FE models to predict the buckling behaviors and the section capacities of the stub beam-columns.

Member dimensions: The actual measuring results of the member dimensions, according to the parameters shown Figure 6, were employed for the FE models.

Meshing: A relatively denser and smaller 4mm×4mm square grid was employed to ensure the accuracy of the simulations. The densely distributed grids were arranged at the corner areas due to the profound strain hardening effect of these areas.

Boundary conditions: Two reference points were respectively located 125mm away from the centroids of two ends, and the coordinates of the two reference points changed according to different loading eccentricities. Use rigid body constraint, and the inlay areas by gypsum should also be taken into consideration. Accordingly, the actual thickness of the gypsum fixed at two ends were measured after tests. Different degrees of freedom were set at the reference points in the FE models so as to be consistent with the test conditions. The overall arrangement of FE models can be seen in Figure 20.

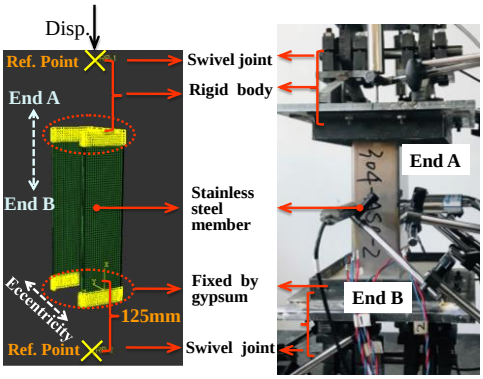

Figure 20 Overall arrangement of the FE models

Analysis step: The Riks analysis step was employed in the FE models to perform the dual nonlinear (material nonlinearity and geometric nonlinearity) analysis during the whole process.

3.1.2 The characteristics of materials

The flat areas and corner areas should be distinguished in the established FE models, and these two areas should be equipped with different material characteristics derived from actual coupon tests. A polyline was obtained as the input stress-strain curves of the material after transforming the engineering stress-strain curves to true stress-strain curves. The Hill yield criterion packaged in ABAQUS was used to definite anisotropy of two materials. The FE models should be translated and rotated when assembling the members, keeping the longitudinal direction of the member consistent with the Axis 1 (X-axis), so as to fit the anisotropy settings mentioned above.

3.1.3 Local imperfection and overall defects

The continuous functions, which contained the imperfection information, were obtained through the actual measurements and a serious of processes. The continuous functions can be operated through the self-compiled program to modify the FE model coordinates in the inp file.

Figure 13 a) presents the simplified local imperfection, linear interpolation was performed on the flanges and quadratic interpolation was performed on the web. In Figure 21, from left to right are perfect member, the member with arbitrary local imperfection (amplified 100 times) and the member with a given local imperfection, respectively

Figure 21 Members with local imperfection

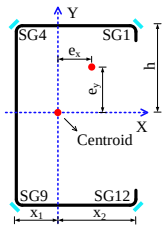

Figure 22 Parameters for overall defects

In this study, the data of four strain gauges in corner areas were used to inversely calculate the equivalent initial loading eccentricity, and the results can be regard as the overall defects (covered installation errors, global imperfection, etc.) of the tests. Figure 22 presents the relative parameters used to calculate the overall defect. E_y can be calculated through the strain data from SG4, SG9 and the Equation 1, Equation 2 (Assume that N is negative). E_x can be obtained through the similar method. All calculation results of overall defects were employed to modify the coordinates of the two reference points.

$$\begin{cases} \sigma_4 = N/A + Nhe_y/I_x - Nx_1e_x/I_y \\ \sigma_9 = N/A - Nhe_y/I_x - Nx_1e_x/I_y \end{cases} \quad (1)$$

$$e_y = (\sigma_4 - \sigma_9)I_x/(2Nh) \quad (2)$$

3.2 Verification

The key responses of the tests and the FE models, such as buckling modes of the members, section capacity, force-displacement curves and force-rotation angle curves, were summarized and then compared to verify the effectiveness and robustness of the FE modeling methods.

3.2.1 Comparison of buckling modes

The buckling modes and overall deformations of all FE column models under their corresponding loading

eccentricity levels were consistent with these of the actual tested members. Figure 23 presents some comparisons between simulation results and tests.

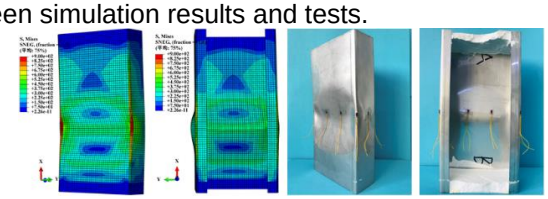

Figure 23 Buckling mode comparisons of 304-BSγ-1

3.2.2 Comparison of ultimate bearing capacities

The ultimate bearing capacity of each FE stub column P_{FE} was in good agreement with its corresponding test result P_u. And all comparison differences between the results of tests and FE models were all within 3%. Some comparisons were shown in Table 2.

Table 2 Comparisons of ultimate bearing capacity

Members	P_u/kN	P_{FE}/kN	P_u/P_{FE}
2205-BSα-2	169.37	173.91	0.974
2205-BSα-3	177.41	178.08	0.996
2205-BSβ-1	147.43	148.88	0.990
2205-BSβ-2	152.39	151.89	1.003
2205-BSγ-1	118.95	120.06	0.991
2205-BSγ-2	122.94	120.72	1.018

3.2.3 *Comparison of force-displacement curves*

The force-displacement curves of FE models fitted well with these of the tests. Some comparisons of force-displacement curves were presented in Figure 24.

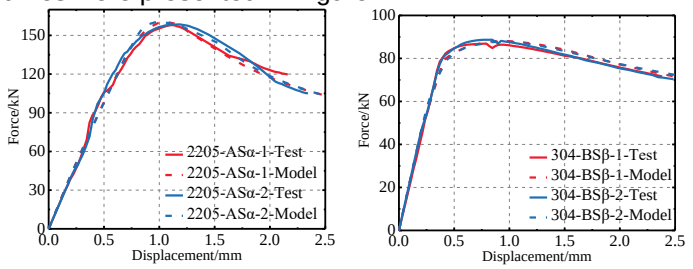

a) 2205-ASα b) 304-BSβ

Figure 24 Comparisons of force-displacement curves

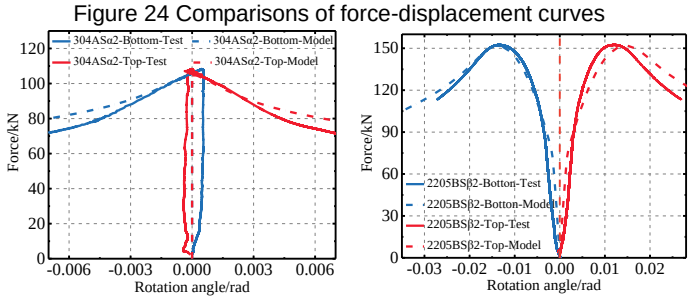

a) 304-ASα-2 d) 2205-BSβ-2

Figure 25 Comparisons of force-rotation angle curves

3.2.4 Comparison of force-rotation angle curves

The force-rotation angle curves of the FE models were in good agreement with that of the tests. Some comparisons of force-rotation angle curves were presented in Figure 25.

4. Parameter study

4.1 Analysis of three influence factors on section capacity

The three influence factors, referring to inlay thickness of the gypsum, local and global imperfection, were investigated based on the calibrated FE models in this subsection. This discussion can provide with a reference for the parameter setting in the following parameter study.

Discussion 1: The influence of inlay thickness and local imperfection on section capacity: The nominal member dimensions with Section A and Section B were employed and the member thickness was taken as 2mm. The modeling method was consistent with the previous FE models. The distribution of the local imperfection was artificially introduced according to the buckling deformations of the two sections, which can be seen in Figure 26.

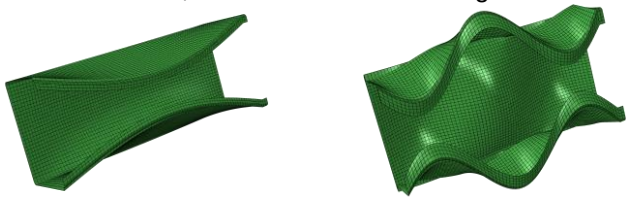

a) Members with Section A a) Members with Section B

Figure 26 Distribution of local imperfection for members (magnified)

Nine inlay thickness levels within the range from 0mm to 32mm were selected. Twelve local imperfection amplitudes within the range from 0.025λt to 1.0λt were introduced. Three loading eccentricity levels defined in previous study were also employed in this subsection. A part of the nondimensionalized results were shown in Figure 27.

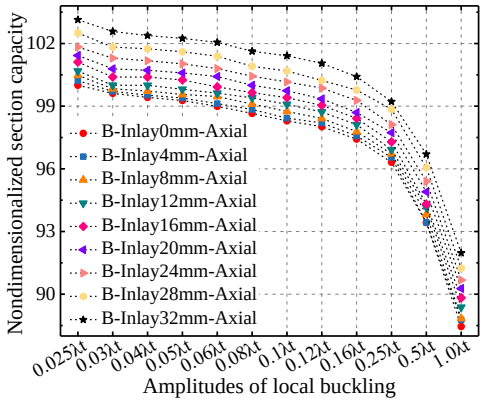

Figure 27 A part of results of Discussion 1

Discussion 2: The influence of distributions and amplitudes of global imperfection on section capacity: Based on the given local imperfection and inlay thickness, different distributions and amplitudes of global imperfection were introduced to the FE models of Section A and Section B. The amplitudes of global imperfection were arranged within the

range from L_0/10000 to L_0/1000, a total of seven amplitude levels. Three loading eccentricity levels were employed in this subsection. The distribution of global buckling was regarded as initial bi-axial bending, which can be presented by the combination of two unidirectional bending. Different unidirectional bending employed in the models were shown in Figure 28. A part of the nondimensionalized results were shown in Figure 29.

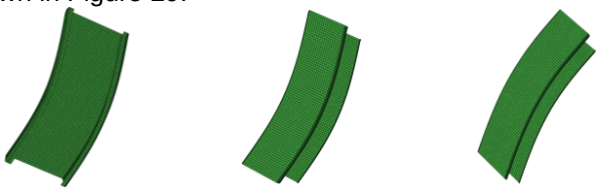

a) About major axis b) About minor axis+ b) About minor axis-

Figure 28 Different unidirectional bending (Amplified)

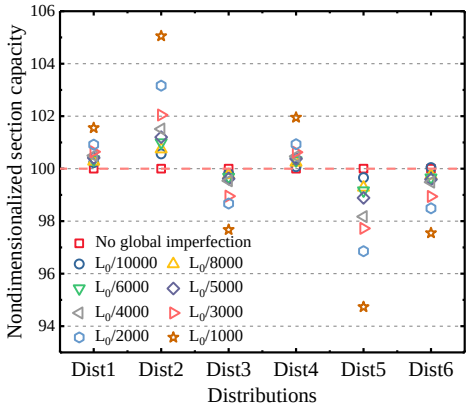

Figure 29 A part of results of Discussion 2

According to the discussions mentioned above, for local imperfection, the distributions presented in Figure 26 were employed in the following parameter study, and the amplitude is 0.08λt; for global imperfection, the most unfavorable combination was selected for modeling and the amplitude was taken as L_0/5000. The inlay thickness was not taken into consideration in the following FE models.

4.2 Parameter analysis

Overall scheme of the parameter analysis: Three types of lipped-C sections were designed in this subsection, these are, the section with a long flange designed to fail by distortional buckling (Type-D1 section), the section with a short flange designed to fail by distortional buckling (Type-D2 section) and the section designed to fail by local buckling (Type-L section). The design goal was consistent with that of the tests. Two alloys (Mat304 and Mat2205), four thickness levels (1mm, 1.85mm, 3mm and 4mm), four slenderness levels (0.8, 1.2, 1.6 and 2.0 for Type-D1 sections and Type-D2 sections; 1.0, 1.5, 2.0 and 2.5 for Type-L sections), and five loading eccentricity levels (Based on the three loading eccentricity levels in the tests, the ratios here are 1.0, 0.75, 0.5, 0.25 and 0, respectively). A total of 480 FE models were established for parameter analysis. CUFSM was used for section selection. The average value of *B/H* of selected Type-D1 sections was 0.779, and that value for selected Type-D2 and Type-L sections was 0.274 and 0.471, respectively. For the member with Type-L section, the member length was taken as three times of its half wave length to reduce global buckling ingredient and to ensure the domination of local buckling. For the member with Type-D1 or Type-D2 section, the member length was taken as one time of its half wave length. The modeling method was consistent with previous study. And two reference points of the FE models were removed to the two end planes.

Results of parameter analysis: The simulation results of the members with Type-D1 section and Type-D2 section under axial compression condition were shown in Figure 30, and the decreasing rules with the increase of the loading eccentricity of the members shown in Figure 30 can be seen in Figure 31.

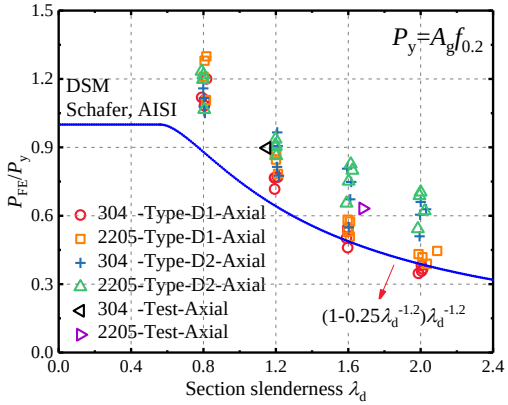

Figure 30 Simulation results of the members with Type-D1 and D2 section under axial compression

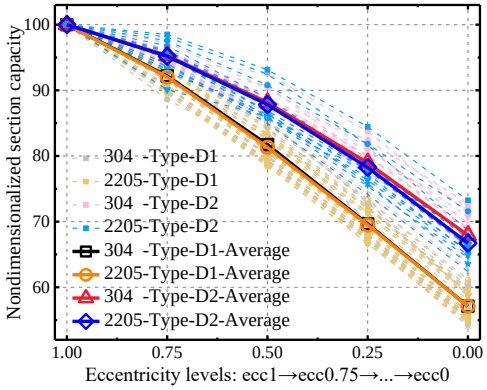

Figure 31 Decreasing rules with the increase of the loading eccentricity levels

5. DSM Prediction of Stainless Steel Lipped-C Stub Beam-columns

In this study, the dominate buckling mode of the designed stub members was distortional buckling or local buckling, and the stability coefficients of all stub members were very close to 1, so the stability of the members was not taken into

consideration. For the members under axial compression condition in this study, the DSM underestimated the section capacity of the members with Type-D2 section. The section capacity of the members with Type-D1 section was underestimated at a relatively lower section slenderness level, and was overestimated at a relatively higher section slenderness level. And the section capacity of the members with Type-L section was overestimated by DSM.

Based on the current DSM expression, a new DSM expression for cold-formed steel beam-columns under combined axial compression and bi-axial bending was put forward by Schafer in 2016 [5]. A normalized *P*-M_1-M_2 space was defined for calculation and different β were used to define different conceptual strength surfaces.

All stub beam-columns in the parameter study were calculated through the new DSM expression. The simulation results and the DSM results were compared, which can be seen in Figure 32. It can be seen through the calculation that, the current DSM expression may not that exactly for the cold-formed stainless steel lipped C stub beam-columns in this study. Accordingly, based on the current DSM expression, the modified expression for the section capacity expression was proposed which suited both stainless steel columns and beam-columns with lipped-C sections.

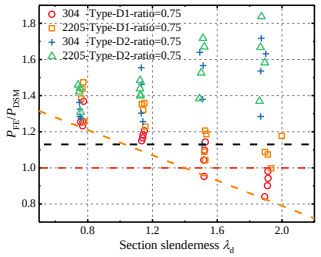

a) Members with Type-D1 and D2 section, ratio=0.75

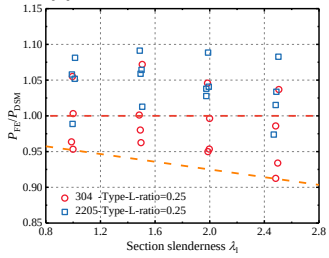

a) Members with Type-L section, ratio=0.25

Figure 32 Comparisons between simulations and the new DSM

The modified DSM expression for members with Type-D1 sections under axial compression was shown in both Equation 3 and Figure 33. The modified DSM expressions for members with Type-D2 and Type-L sections under axial compression were shown in Equation 4 and Equation 5, respectively.

$$P_d = \begin{cases} Af_y & \lambda_d < 0.801 \\ (1-0.2\lambda_d^{-1.5})\lambda_d^{-1.5}Af_y & \lambda_d > 0.801 \end{cases} \quad (3)$$

$$P_d = \begin{cases} Af_y & \lambda_d < 0.901 \\ (1-0.1\lambda_d^{-1.2})\lambda_d^{-1.2}Af_y & \lambda_d > 0.901 \end{cases} \quad (4)$$

$$P_l = \begin{cases} Af_y & \lambda_d < 0.490 \\ (1-0.25\lambda_l^{-1.0})\lambda_l^{-1.0}Af_y & \lambda_d > 0.490 \end{cases} \quad (5)$$

The modified DSM expression for members with Type-D1 sections under combined axial compression and uniaxial bending was shown in Equation 6. And the comparisons of the results between FE models and revised DSM expressions can be shown in Figure 34.

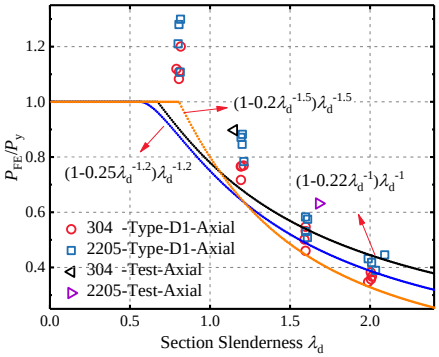

Figure 33 Modified DSM expression for members with Type-D1 section under axial compression

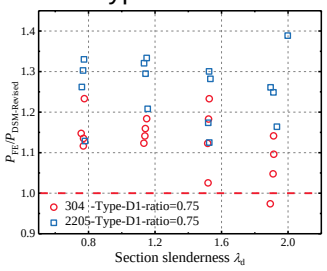

a) Members with Type-D1 section, ratio=0.75

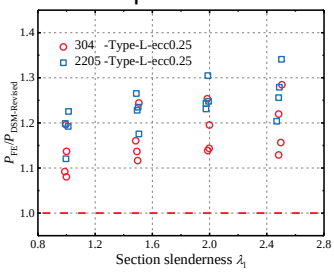

a) Members with Type-L section, ratio=0.25

Figure 34 Comparisons between simulations and the revised DSM

The modified DSM expressions for members with Type-D2 and Type-L sections under combined axial compression and uniaxial bending were shown in Equation 7 and Equation 8, respectively.

$$\beta_d = \begin{cases} \beta_y & \lambda_d \le 0.801+0.112\sin\phi_{PM} \\ \left(1-c_1\lambda_d^{-2c_2}\right)\lambda_d^{-2c_2}\beta_y & \lambda_d > 0.801+0.112\sin\phi_{PM} \end{cases} \quad (6)$$

$$c_1 = 0.2-0.03\sin\phi_{PM} \quad c_2 = 0.75-0.1\sin\phi_{PM}$$

$$\beta_d = \begin{cases} \beta_y & \lambda_d \le 0.901+0.112\sin\phi_{PM} \\ \left(1-c_1\lambda_d^{-2c_2}\right)\lambda_d^{-2c_2}\beta_y & \lambda_d > 0.901+0.112\sin\phi_{PM} \end{cases} \quad (7)$$

$$c_1 = 0.1-0.03\sin\phi_{PM} \quad c_2 = 0.6-0.1\sin\phi_{PM}$$

$$\beta_l = \begin{cases} \beta_y & \lambda_l \le 0.490 \\ \left(1-0.25\lambda_l^{-1.0}\right)\lambda_l^{-1.0}\beta_y & \lambda_l > 0.490 \end{cases} \quad (8)$$

5. Conclusions

In this study, the buckling behaviors and the section capacity of cold-formed stainless steel lipped-C stub columns under combined axial compression and uniaxial bending were investigated through experimental investigation, numerical simulation and theoretical study. And the conclusions were listed as follows:

Two sets of sections were designed to fail by distortional buckling or local buckling, all of the 24 test members achieved their expected buckling modes.

The FE modeling method can be verified by the comparisons of the key responses between the FE models and the tests. The buckling modes, overall deformations, force-displacement curves and force-rotation angle curves of the FE models were in good agreement with those of the tests.

The influence of inlay thickness of the two ends, amplitude and distribution of local and global imperfection on section capacity of stub members were obtained through simulations. A total of 480 FE models, containing three kinds of sections, were performed to provide with reference for theoretical study.

Based on the current DSM expression, the revised DSM expression for section capacity prediction was proposed which suited both stainless steel columns and beam-columns of lipped-C sections.

References

[1] Gardner, L. The use of stainless steel in structures. Progress in Structural Engineering and Materials, 7(2), 45-55, 2005.

[2] Baddoo, N. R. Stainless steel in construction: A review of research, applications, challenges and opportunities. Journal of Constructional Steel Research, 64(11), 1199-1206, 2008.

[3] Gedge, G. Structural uses of stainless steel—buildings and civil engineering. Journal of constructional steel research, 64(11), 1194-1198, 2008.

[4] Niu S. Interaction Buckling of Cold-Formed Stainless Steel Beams. Sydney, Harbin: The University of Sydney, Harbin Institute of Technology, 2014.

[5] Torabian S, Schafer B W, et al. Direct Strength Prediction of Cold-Formed Steel Beam-Columns. Baltimore, MD: Johns Hopkins University, 2016.

[6] Zheng B. Investigations on the Key Problems in the Mechanical properties of Cold Formed Stainless Steel Structures. Nanjing, China: Southeast University, 2017.

[7] Gardner L, Nethercot D A. Experiments on Stainless Steel Hollow Sections – Part 1: Material and Cross-Sectional Behavior. Journal of Constructional Steel Research, 2004, 60(9):1291-1318.

[8] Lecce M. Distortional Buckling of Stainless Steel Sections. Sydney, Australia: The University of Sydney, 2006.

[9] Becque J. The Interaction of Local and Overall Buckling of Cold-Formed Stainless Steel Columns. Sydney, Australia: The University of Sydney, 2008.

[10] Johnson A L, Winter G. Behavior of Stainless Steel Columns and Beams. Journal of the Structural Division, ASCE, 1966, 92:ST5:97-118.

[11] Li Z, Schafer B W. Buckling Analysis of Cold-Formed Steel Members with General Boundary Conditions using CUFSM: Conventional and Constrained Finite Strip Methods. 20th International Specialty Conference on Cold-Formed Steel Structures, St. Louis, MO: Missouri University of Science and Technology, 2010:17-31.

[12] Walker A C, Design and Analysis of Cold-Formed Sections. London: International Textbook Company Ltd., 1975.